

ML in Astrophysical Turbulence I: Predicting Prestellar Cores in Magnetized Molecular Clouds using eXtreme Gradient Boosting

NIKHIL P. S. BISHT ¹ AND DAVID C. COLLINS ¹

¹*Department of Physics, Florida State University, Tallahassee, Florida, USA*

ABSTRACT

Giant Molecular Clouds (GMCs) are dominated by supersonic turbulence, creating a complex network of shocks and filaments that regulate star formation. While the global inefficiency of star formation is well-observed, predicting exactly which gas parcels within a turbulent cloud will collapse to form stars remains a challenge. In this work, we present a supervised machine learning framework to forecast the Lagrangian history of prestellar cores in magnetohydrodynamic (MHD) turbulence. We utilize Extreme Gradient Boosting (XGBoost) to train a regression model on the trajectories of ~ 2.1 million tracer particles evolved within a self-gravitating, turbulent MHD simulation.

By mapping the instantaneous phase-space state (position, velocity, and density) of gas parcels to their future coordinates, our model successfully predicts the 3D evolution of star-forming cores over a horizon of ~ 0.45 Myr ($0.25 t_{\text{ff}}$). We achieve a global coefficient of determination of $R^2 > 0.99$ and demonstrate that the model captures the non-linear convergent flows characteristic of gravitational collapse. Crucially, we show that local phase-space information alone is sufficient to distinguish between transient density fluctuations and bound collapsing cores. This data-driven approach offers a computationally efficient alternative to traditional sink-particle algorithms and provides a pathway for developing high-fidelity subgrid models for galaxy-scale simulations.

Keywords: Molecular clouds (1072) — Regression (1914) — Magnetohydrodynamical simulations (1966)

1. INTRODUCTION

The formation of stars is the fundamental driver of galaxy evolution, regulating the interstellar medium (ISM) through feedback and enriching the universe with heavy elements. Despite its importance, the precise mechanism that regulates the rate of star formation remains one of the central problems in astrophysics. Observations indicate that star formation is surprisingly inefficient; only 1% – 2% of a molecular cloud’s mass is converted into stars per free-fall time ($\epsilon_{\text{ff}} \approx 0.01$) (Krumholz & McKee 2005; Krumholz & Tan 2007). This inefficiency is generally attributed to the interplay between self-gravity, which promotes collapse, and supersonic turbulence and magnetic fields, which provide support and shear apart potential star-forming regions (McKee & Ostriker 2007; Federrath & Klessen 2012).

Giant Molecular Clouds (GMCs) are the primary nurseries for this process. Spanning scales from tens of parsecs ($\sim 10^{17}$ m) down to the size of prestellar cores at about 0.1 parsecs ($\sim 3 \times 10^{15}$ m), these clouds represent a chaotic environment where gas spans orders

of magnitude in density and temperature. The standard paradigm suggests that supersonic turbulence creates a complex network of shocks and filaments (Larson 1981; Mac Low & Klessen 2004). Within this turbulent cascade, transient overdensities form and dissolve, but only those fluctuations that are gravitationally bound and magnetically supercritical (a rare subset) succeed in collapsing to form prestellar cores (Shu 1977; Padoan & Nordlund 2002; Crutcher 2012).

Once these cores collapse and protostars ignite, they inject significant energy back into their environment. Radiative feedback (e.g., UV heating and photoionization) and protostellar outflows play a critical role in regulating the global star formation efficiency by dispersing the surrounding gas and halting further accretion (McKee & Ostriker 2007). However, as this study focuses strictly on the kinematic origins and the initial turbulent fragmentation of the *prestellar* phase which is prior to the onset of stellar ignition, we approximate the gas thermodynamics using an isothermal equation of state and intentionally omit radiative feedback mechanisms. This isolates the purely gravity-driven turbu-

lence and advective rules our machine learning model aims to learn.

Observational surveys using tracer molecules (e.g., ^{12}CO , NH_3 , N_2H^+) and dust continuum emission have provided a wealth of data regarding the morphology of these regions (Alatalo et al. 2013; Evans et al. 2009). Recent high-resolution campaigns with ALMA and observational analysis of cloud statistics (Chevance et al. 2022; Sahu et al. 2021) have highlighted the environmental dependence of core formation. However, observations suffer from projection effects (2D snapshots of 3D structures) and a lack of temporal evolution. We observe the "before" (diffuse gas) and "after" (protostars), but the critical dynamic phase of collapse is often obscured or ambiguous.

To bridge this gap, high-resolution Magnetohydrodynamic (MHD) simulations have become indispensable. Codes such as ENZO, FLASH, and AREPO allow us to model the non-linear equations of fluid dynamics coupled with gravity and magnetic fields (Bryan et al. 2014; Fryxell et al. 2000; Weinberger et al. 2020). While simulations provide full 6D phase-space information, identifying the Lagrangian history of star-forming gas, i.e., tracing the specific parcels of gas that will eventually become stars, remains a non-trivial data analysis challenge. Traditional methods often rely on thresholding (e.g., density cutoffs) or sink particles (Bate et al. 1995; Federrath et al. 2010; Wang et al. 2009), which identify collapse only *after* it has become irreversible.

In recent years, Machine Learning (ML) has emerged as a powerful tool for analyzing the complex, high-dimensional datasets produced by astrophysical simulations. ML techniques have been successfully applied to estimate halo masses (Ntampaka et al. 2015), classify galaxy morphologies (Dieleman et al. 2015), and infer physical parameters from turbulent fields (Peek & Burkhart 2019). In the context of star formation, recent works have begun to utilize Deep Learning to classify young stellar objects (Tan et al. 2024) and identify structures in molecular line data. However, most efforts focus on Convolutional Neural Networks (CNNs) applied to image data.

In this work, we present a novel approach focusing on the *Lagrangian* dynamics of the gas. We treat the prediction of core collapse not as an image recognition task, but as a tabular supervised learning problem. We utilize **XGBoost** (Extreme Gradient Boosting), a decision-tree-based ensemble method (Chen & Guestrin 2016), to analyze the trajectories of passive tracer particles in a turbulent MHD simulation. Unlike "black box" neural networks, tree-based models are highly effective for tabular physical data (density, velocity, magnetic field) and

offer interpretability regarding feature importance. Our goal is to answer a specific question: *Given the instantaneous state of a gas parcel in a turbulent cloud, can we predict its future coordinate and accretion fate?*

This paper is structured as follows. Section 2 details the MHD simulation setup, the tracer particle methodology, and the data pipeline. Section 3 describes the problem formulation and the XGBoost architecture. Section 4 presents the model performance, including temporal generalization tests and core trajectory reconstruction. We discuss the physical implications of our findings in Section 5 and conclude in Section 6.

2. SIMULATIONS AND DATA

2.1. Turbulence Box Simulations

We utilize the open-source adaptive mesh refinement (AMR) code ENZO (Bryan et al. 2014) with the constrained transport magnetohydrodynamics (MHD) module (Collins et al. 2010). The code adaptively increases resolution as the collapse proceeds, triggering refinement whenever the local Jeans length, $L_J = c_s(\pi/G\rho)^{1/2}$, is resolved by fewer than 16 zones. The primary solver employs a higher-order Godunov method, utilizing the linear reconstruction method of Li et al. (2008), the HLLD Riemann solver of Mignone (2007), and the electric field correction of Gardiner & Stone (2005) to maintain the divergence-free constraint of the magnetic field ($\nabla \cdot \mathbf{B} = 0$).

To track the gas parcels in a Lagrangian framework, we include passive tracer particles that follow the flow via a piecewise linear interpolation of the grid velocity field (see Bryan et al. 2014; Collins et al. 2023).

Initial conditions are generated following the procedure of Mac Low (1999): we initialize a periodic turbulent box with uniform density ρ_0 and uniform magnetic field B_0 . We inject kinetic energy at large scales, allowing it to cascade to smaller scales via non-linear interactions until a statistically steady state is achieved. At this point, we activate self-gravity, insert uniformly spaced tracer particles, and allow the gas to collapse. The simulation is scale-free and characterized by the sonic Mach number \mathcal{M} , the virial parameter α_{vir} , and the plasma β_0 :

$$\mathcal{M} = \frac{v_{\text{rms}}}{c_s} = 9 \quad (1)$$

$$\alpha_{\text{vir}} = \frac{5v_{\text{rms}}^2}{3G\rho_0 L_0} = 1 \quad (2)$$

$$\beta_0 = \frac{8\pi c_s^2 \rho_0}{B_0^2} = 0.2 \quad (3)$$

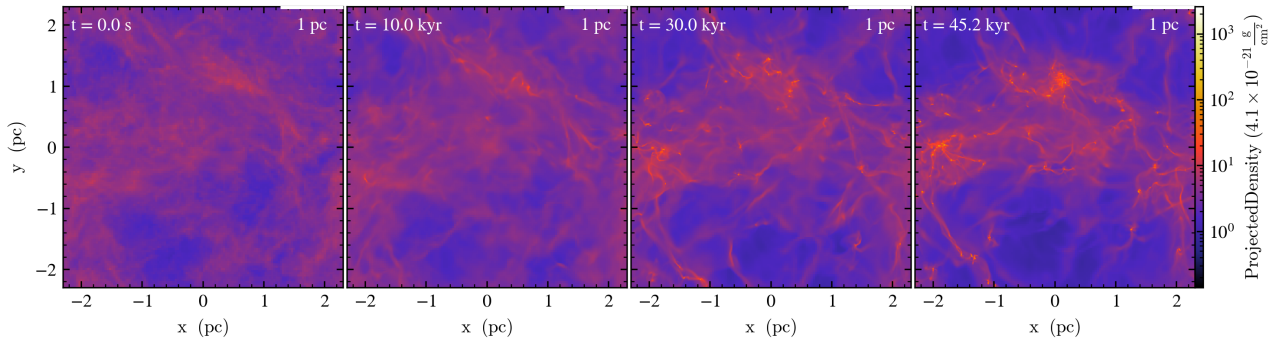


Figure 1. Evolution of the turbulent density field. We show the column density projection (Σ) of the simulation box at four evolutionary stages, ranging from the initial turbulent driving phase ($t = 0$) to the onset of widespread core collapse ($t \approx t_{\text{ff}}$).

Table 1. Dataset *MCDS1*

ID	Frame	x_i	y_i	z_i	$v_{x,i}$	$v_{y,i}$	$v_{z,i}$	ρ_i	x_f	y_f	z_f
		[code units]			[code units]			[code units]	[code units]		
4	20	0.957	0.049	0.020	-9.77	5.67	2.12	0.17	0.860	0.133	0.041
5	20	0.969	0.049	0.021	-9.18	5.61	2.21	0.57	0.871	0.124	0.050
6	20	0.982	0.049	0.021	-8.68	5.69	2.41	0.75	0.884	0.118	0.057
15	20	0.055	0.044	0.038	-8.73	4.82	4.90	0.45	0.966	0.087	0.099
17	20	0.079	0.035	0.043	-7.94	3.90	5.31	0.46	0.991	0.081	0.112

where v_{rms} is the root-mean-square velocity, c_s is the sound speed, and L_0 is the box size (approx. 3.2 pc in physical units). The magnetic field is initially uniform in the \hat{x} direction.

The simulation evolves for approximately one free-fall time, $t_{\text{ff}} = \sqrt{3\pi/32G\rho_0}$. We initialize 128^3 tracer particles (one per root-grid zone), totaling 2,097,152 particles. Tracers are evolved using a second-order predictor-corrector scheme where the particle position is updated as $\mathbf{x}^{n+1} = \mathbf{x}^n + \Delta t \mathbf{v}_p$. Refinement continues for 4 levels, yielding a maximum effective resolution of 2048^3 . Further details on the simulation suite can be found in (Collins et al. 2023; Collins et al. 2024).

2.2. Data Extraction and Preparation

The simulation state is archived at high frequency, resulting in 121 snapshots spanning $1.0 t_{\text{ff}}$. Each snapshot represents a physical time interval of approximately 0.015 Myr. For every snapshot i , we extract the full phase-space state for each tracer particle: position \mathbf{x}_i , velocity \mathbf{v}_i , and local gas density ρ_i . This raw collection constitutes our base dataset, hereafter *MCDS0*.

As the turbulence decays and gravity takes over, the gas fragments into high-density islands ($n \sim 10^5 - 10^8 \text{cm}^{-3}$) roughly a few hundred AU in size. We refer to these structures as *pseudo-cores*. To identify these regions, we employ a dendrogram algorithm (Rosolowsky

et al. 2008) on the final simulation snapshot ($t = t_{\text{ff}}$), identifying peaks with density $n > 10^4 n_0$. We then tag all tracer particles located within the densest zones of these peaks ($n > n_{\text{peak}}^{3/4}$) as "core particles."

This selection procedure isolates $\sim 117,364$ particles ($\sim 5.6\%$ of the total population) that successfully accrete onto prestellar cores. We partition the dataset into two subsets: *MCDS0-Core* (particles ending in cores) and *MCDS0-NonCore* (particles that remain in the diffuse medium).

To prepare the data for supervised learning, we transform the time-series data into a tabular regression format. The objective of our model Φ is to map the state vector of a particle at time t , \mathbf{x}_t , to its future position at time $t + \Delta T$. We construct the training dataset, *MCDS1*, by pairing the input features at snapshot i with the target coordinates at snapshot $i + \Delta_{\text{frame}}$. The resulting feature vector for each sample is $\mathbf{X} = \{\text{ID}, \text{Frame}, x, y, z, v_x, v_y, v_z, \log_{10} \rho\}$, and the target vector is $\mathbf{Y} = \{x_{t+\Delta T}, y_{t+\Delta T}, z_{t+\Delta T}\}$.

A critical hyperparameter in this formulation is the prediction horizon, ΔT . A very small ΔT renders the problem trivial (linear advection), while a very large ΔT makes the turbulent mapping non-unique and chaotic. We select a lag of $\Delta_{\text{frame}} = 30$ snapshots, which corresponds to $\Delta T \approx 0.45$ Myr. This value was chosen to match the integral time scale of the turbulence, ensuring

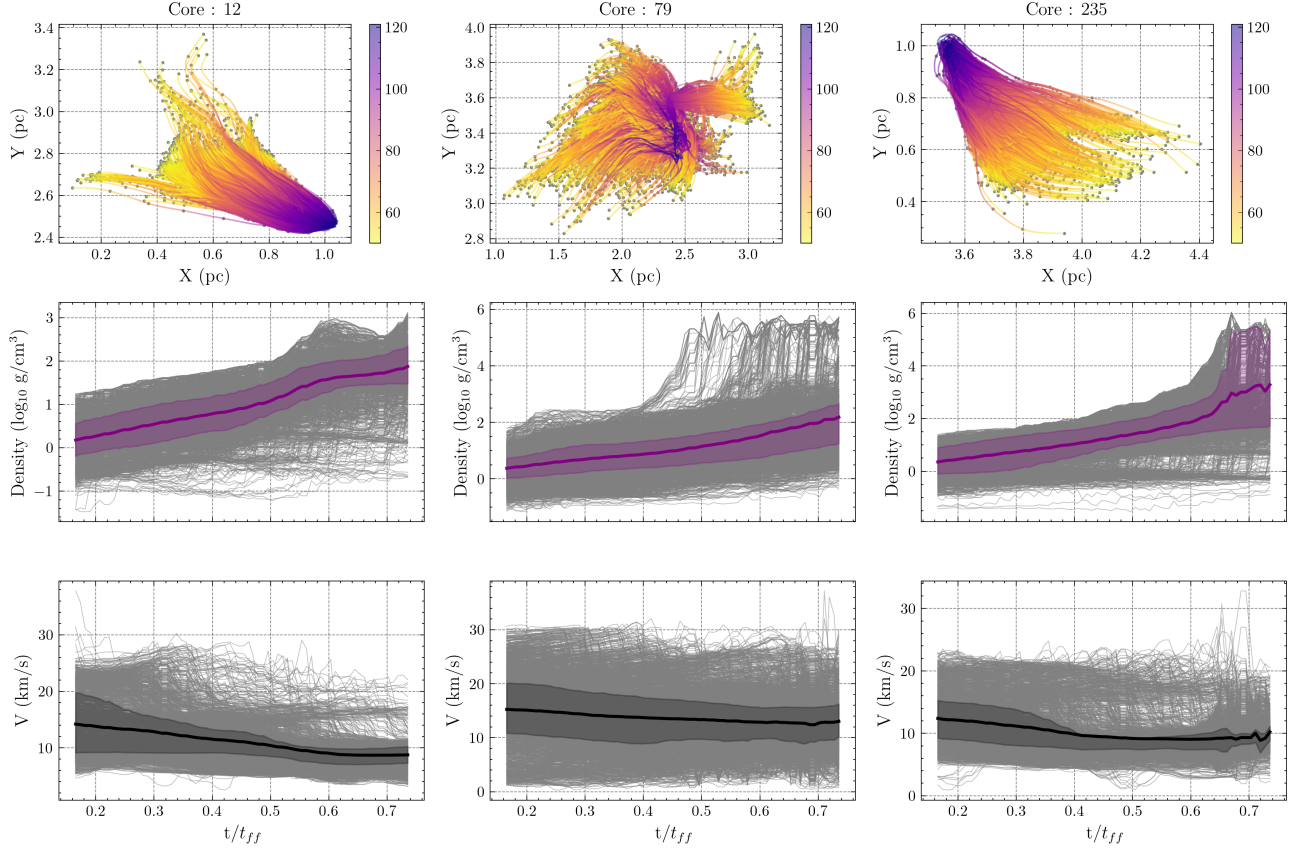


Figure 2. Evolution of three representative prestellar cores. **Top:** Projected trajectories of tracer particles belonging to each core from $t = 0.5t_{ff}$ (yellow) to $t = 1.0t_{ff}$ (purple). **Middle:** Evolution of the local gas density surrounding the tracers. **Bottom:** Evolution of the velocity magnitude. The solid lines represent the median value for the core’s constituent particles, while the shaded regions indicate the 25th-75th percentile range. As collapse proceeds, density increases rapidly while the velocity dispersion decreases, indicating coherent infall.

the model predicts evolution over physically significant dynamical times (see Section 2.3).

2.3. Statistical Analysis of Features

Before training, we analyze the statistical properties of the *MCDS1-Core* dataset. Figure 2 illustrates the phase-space evolution of three distinct cores. In the early phase ($t \approx 0.5t_{ff}$), tracers are spatially extended and possess high velocity dispersion. As collapse ensues, the trajectories converge (top row), density rises by orders of magnitude (middle row), and the velocity distribution narrows (bottom row), signifying the transition from turbulent support to gravitational infall.

Figure 3 shows the global probability density functions (PDFs) for density and velocity at three epochs. The density PDF develops a power-law tail at late times, a hallmark of gravitational collapse (Krumholz & McKee 2005; Collins et al. 2012). We also compute the Pearson correlation matrix for the input features (Figure 4, top). As expected, the final position is most strongly correlated with the initial position. However, significant

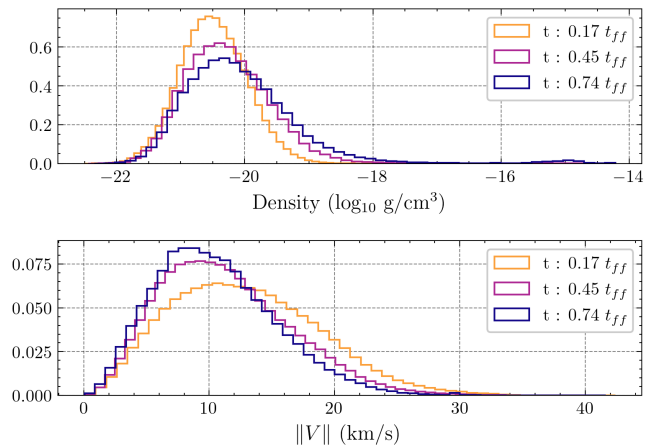


Figure 3. Global evolution of gas properties. **Top:** Probability distribution function (PDF) of log-density at frames 20 (yellow), 55 (purple), and 90 (blue). **Bottom:** PDF of velocity magnitude. The development of a high-density tail and the sharpening of the velocity peak indicate the formation of gravitationally bound structures.

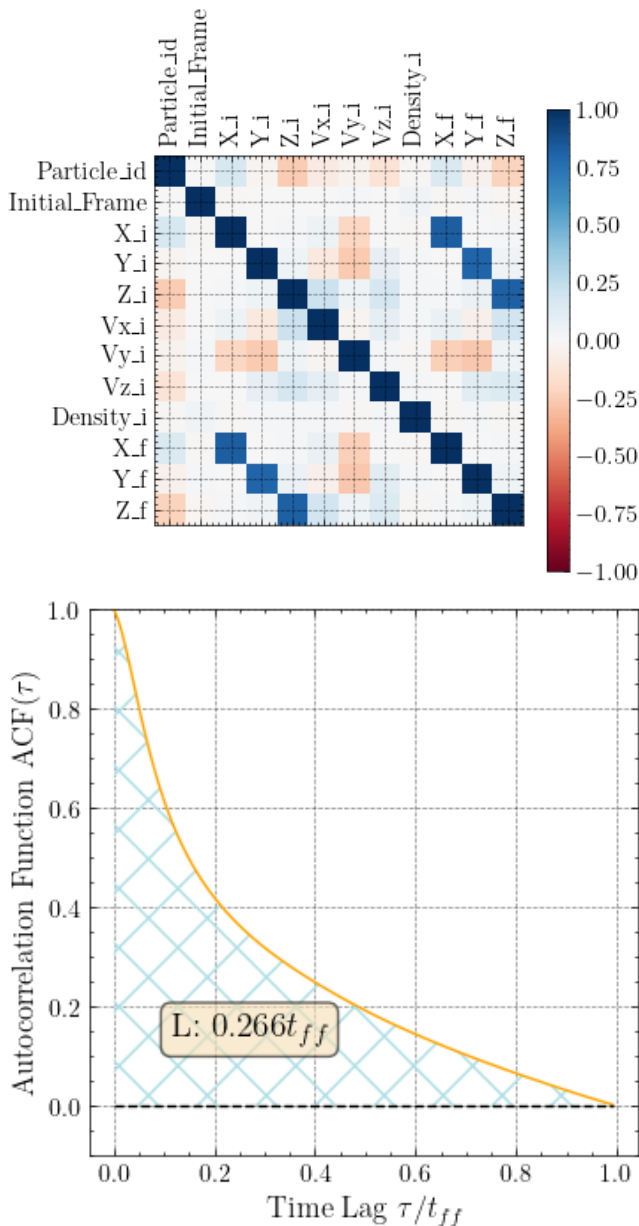


Figure 4. Top: Pearson correlation matrix for the training features in *MCDS1*. **Bottom:** Temporal autocorrelation function of the density field. The integral of this curve yields the turbulent correlation time, which informs our choice of the prediction horizon ΔT .

non-zero correlations exist between density and velocity, which the machine learning model will exploit to improve upon simple ballistic extrapolation.

To rigorously justify our choice of $\Delta T = 30$ frames, we compute the integral time scale of the turbulence. We define the density fluctuation field $\delta(x, t) = \rho(x, t) - \bar{\rho}$ and calculate its normalized temporal autocorrelation

function (ACF):

$$\mathcal{ACF}(\tau) = \frac{\langle \delta(x, t) \delta(x, t + \tau) \rangle_{x,t}}{\langle \delta(x, t)^2 \rangle_{x,t}} \quad (4)$$

The integral time scale L_τ is obtained by integrating the ACF:

$$L_\tau = \int_0^{t_{ff}} \mathcal{ACF}(\tau) d\tau \quad (5)$$

As shown in Figure 4 (bottom), this integral converges to approximately $0.25 t_{ff}$, which corresponds to ~ 0.45 Myr or 30 simulation snapshots. This confirms that our prediction window matches the coherence time of density structures in the flow.

3. METHODS

3.1. Problem Formulation

We formulate the prediction of prestellar core formation as a supervised regression problem. Let the state of a tracer particle at time t be represented by a feature vector $\mathbf{x}_t \in \mathbb{R}^n$, containing the local physical properties (position, velocity, density). Our objective is to learn a mapping function $\Phi: \mathbb{R}^n \rightarrow \mathbb{R}^3$ that predicts the particle's spatial coordinates at a future time $t + \Delta T$.

Formally, given a dataset $\mathcal{D} = \{(\mathbf{x}_i, \mathbf{y}_i)\}_{i=1}^N$, where \mathbf{y}_i is the true position of the i -th particle at the target time, we seek to optimize the function Φ such that the expected loss is minimized:

$$\Phi^* = \underset{\Phi}{\operatorname{argmin}} \sum_{i=1}^N L(\mathbf{y}_i, \Phi(\mathbf{x}_i)) + \Omega(\Phi) \quad (6)$$

where L is the loss function quantifying the error between the prediction and the ground truth, and Ω is a regularization term to prevent overfitting. Unlike simple linear advection schemes, the mapping Φ must capture the non-linear dynamics of magnetohydrodynamic turbulence, including shocks and gravitational acceleration.

3.2. Extreme Gradient Boosting (XGBoost)

To approximate Φ , we employ Extreme Gradient Boosting (XGBoost) (Chen & Guestrin 2016), an efficient implementation of the Gradient Boosted Decision Tree (GBDT) algorithm. We select a tree-based ensemble over traditional linear regression or simple neural networks for two reasons: (1) Decision trees naturally handle the sharp discontinuities present in supersonic turbulent flows (shocks), and (2) they are invariant to the monotonic scaling of features, requiring less pre-processing of variables like density, which spans many orders of magnitude.

The model approximates the target variable by summing the outputs of K regression trees:

$$\hat{\mathbf{y}}_i = \Phi(\mathbf{x}_i) = \sum_{k=1}^K f_k(\mathbf{x}_i), \quad f_k \in \mathcal{F} \quad (7)$$

where \mathcal{F} is the space of regression trees. The model is trained additively: at each step t , a new tree f_t is added to minimize the residual errors of the prior ensemble. The objective function at step t is:

$$\mathcal{L}^{(t)} = \sum_{i=1}^N l(\mathbf{y}_i, \hat{\mathbf{y}}_i^{(t-1)} + f_t(\mathbf{x}_i)) + \Omega(f_t) \quad (8)$$

The regularization term $\Omega(f)$ penalizes model complexity to ensure physical generalizability:

$$\Omega(f) = \gamma T + \frac{1}{2} \lambda \|w\|^2 \quad (9)$$

where T is the number of leaves in the tree and w represents the leaf weights. We tune the hyperparameters γ (minimum loss reduction) and λ (L2 regularization) via the grid search described in Section 4.

3.3. Model Evaluation Metrics

We evaluate the regression performance using four statistical metrics. To account for the periodic boundary conditions of our simulation box (where a position of 1.0 is equivalent to 0.0), we define the periodic distance function \mathcal{P} :

$$\mathcal{P}(a, b) = \min(|a - b|, 1 - |a - b|) \quad (10)$$

1. Periodic Mean Absolute Error (P-MAE):

The primary metric for optimizing the model.

$$\text{P-MAE} = \frac{1}{N} \sum_{i=1}^N \mathcal{P}(\mathbf{y}_i, \hat{\mathbf{y}}_i) \quad (11)$$

2. Periodic Coefficient of Determination (R_p^2):

Measures the proportion of variance in the particle trajectories captured by the model.

$$R_p^2 = 1 - \frac{\sum \mathcal{P}(\mathbf{y}_i, \hat{\mathbf{y}}_i)^2}{\sum \mathcal{P}(\mathbf{y}_i, \bar{\mathbf{y}})^2} \quad (12)$$

3. Cross-Validation Uncertainty (σ_{CV}):

To estimate the model’s reliability on unseen data, we employ repeated k-fold cross-validation (10 folds, 3 repeats) (Stone 1974). The standard deviation of the MAE across these folds, σ_{CV} , serves as the systematic uncertainty of our model.

4. Bounded Accuracy Fraction: To quantify the reliability of our model beyond global averages, we introduce the *Bounded Accuracy Fraction* (A_k). Unlike the Coefficient of Determination (R^2), which can be heavily influenced by outliers, A_k measures the percentage of test particles whose prediction error lies within a strict physical tolerance. We define this tolerance based on the intrinsic uncertainty of the model, estimated via the mean absolute error of the cross-validation set ($\sigma_{\text{CV}} = \text{MAE}_{\text{CV}}$). The Bounded Accuracy for a tolerance factor k is defined as:

$$A_k = \frac{1}{N} \sum_{i=1}^N \mathbb{I}(|\mathbf{y}_i - \hat{\mathbf{y}}_i| < k \cdot \sigma_{\text{CV}}) \quad (13)$$

where \mathbb{I} is the indicator function. In this work, we report results for $k = 3$. This corresponds to a 3σ confidence interval, a standard threshold in physical sciences for robust statistical significance. A high value of A_3 indicates that the model’s errors are well-behaved and that ”catastrophic” failures (predictions deviating by $> 3 \times$ the typical error) are rare.

4. RESULTS

4.1. Hyperparameter Optimization

We construct tree-boosted regression models using the **XGBoost** framework. To ensure our model generalizes well to unseen turbulent flow configurations and avoids overfitting to specific simulation snapshots, we perform a rigorous hyperparameter optimization. We utilize repeated k-fold cross-validation (3 repeats, 10 folds) on a training subset of 2.3×10^6 particle trajectories. This ensures that the validation fold is strictly disjoint from the training data, mimicking the evaluation of an unknown physical state.

The hyperparameter search space was selected to balance model complexity with computational efficiency, given the high-dimensional nature of turbulent flows:

- **n_estimators** $\in [500, 1500]$: The number of boosted trees. We test lower bounds to avoid underfitting complex shocks and upper bounds to limit computational overhead.
- **eta** (Learning Rate) $\in [0.01, 0.3]$: Controls the step size of the gradient descent. Lower values (0.01) generally yield more robust models but require more trees.
- **gamma** $\in [0.5, 5]$: The minimum loss reduction required to make a further partition on a leaf node.

Table 2. Hyperparameter gridsearch results best and worst models

Model	Hyperparameters					Mean Absolute Error		Time Taken	
	n_estimators	eta	gamma	subsample	max_depth	(pc)		(s)	
						Mean (std)	Mean (std) Fitting	Mean (std) Scoring	
Model A (Optimized)	500	0.1	0.5	1.0	8	0.040926 (0.000101)	170.4 (20.9)	2.8 (0.8)	
Model B (Intermediate)	1000	0.01	1	0.4	7	0.054045 (0.000069)	594.7 (109.4)	20.9 (7.8)	
Model C (Baseline)	500	0.01	5	0.4	7	0.070951 (0.000110)	424.6 (127.2)	6.5 (2.9)	

Higher values act as regularization, preventing the model from fitting numerical noise in the low-density regions.

- **subsample** $\in [0.4, 1.0]$: The fraction of observations to be randomly sampled for each tree. Subsampling introduces randomness that improves robustness against local outliers in the simulation.
- **max_depth** $\in [6, 8]$: Constrains the depth of individual trees. We cap this at 8 to prevent the model from memorizing specific particle trajectories.

The results of the grid search are summarized in Table 2. We designate the highest performing configuration as **Model A (Optimized)**, which utilizes a high subsample rate (1.0) and moderate depth (8), achieving the lowest Mean Absolute Error (MAE). Models with aggressive regularization (high **gamma**, low **eta**) generally underperformed (**Model C**), suggesting that the complexity of turbulent core collapse requires a model with sufficient capacity to capture fine-grained phase-space correlations.

4.2. Global Model Performance & Reliability

Having identified the optimal hyperparameter configuration (Model A) and two reference points (Intermediate Model B and Baseline Model C), we evaluate their global predictive capabilities. A critical question is not just minimizing the mean error, but ensuring the model is reliable across different physical regimes (e.g., high-density cores vs. diffuse gas).

Figure 5 compares the performance of the three model tiers. **Model A (Optimized)** achieves a global MAE of 0.0314 pc ($R^2 = 0.9988$). In contrast, the **Baseline Model C** (characterized by high regularization and shallow trees) shows a 40% higher error rate ($MAE \approx 0.069$ pc).

To further quantify the predictive value of our chosen features, we conducted an ablation study by training a reduced "Position-Only" model, restricted strictly to spatial coordinates ($\mathbf{x}_i = \{x, y, z\}$) and excluding velocity and density. While this reduced model achieved

reasonable accuracy for the background advection of diffuse non-core gas, its performance degraded significantly in the high-density core regimes. Without local velocity and density information, the model failed to anticipate the non-linear acceleration driven by gravitational collapse, confirming that the full phase-space vector is essential for accurately forecasting star formation dynamics.

4.3. Temporal Generalization and Cross-Simulation Robustness

While global error metrics provide a baseline for model performance, the true test of a predictive physical model is its ability to forecast future states and generalize to unseen initial conditions. To evaluate this, we perform a "future frame" extrapolation test. The model, trained strictly on the early evolutionary phase ($t \in [0.167, 0.67]t_{ff}$) of our fiducial simulation (*u501*), is tasked with predicting the phase-space coordinates of particles in a future time interval ($t \in [0.925, 1]t_{ff}$).

Figure 6 is the central result of this temporal validation. The top panel displays the distribution of the Euclidean distance error ($|\mathbf{x}_{\text{true}} - \mathbf{x}_{\text{pred}}|$) for the XGBoost predictions (purple) compared against a "No-Motion Baseline" (red crosses). The No-Motion baseline assumes particles remain static over the prediction horizon (ΔT), effectively measuring the inherent bulk flow of the gas. Beating this baseline is the fundamental criterion for proving that the machine learning algorithm has learned the physical kinematics of the system rather than merely applying a persistence forecast. As shown, the model significantly outperforms the baseline across all future frames. While the prediction error naturally grows as the simulation evolves further from the training window which is an unavoidable consequence of the positive Lyapunov exponents in chaotic turbulent flows, the XGBoost predictions remain tightly bounded and physically realistic.

4.3.1. Generalization to Varying Magnetic Field Strengths

To rigorously test the generalizability of our learned phase-space correlations, we deploy the model on a com-

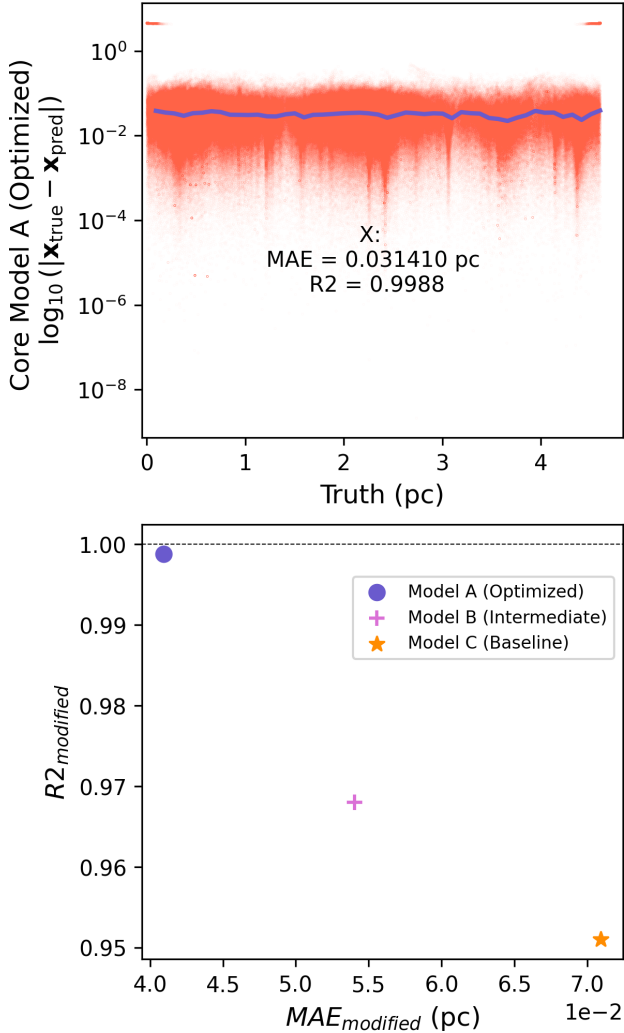


Figure 5. Performance comparison of the Optimized (Model A), Intermediate (Model B), and Baseline (Model C) architectures. **Top:** Prediction-Truth for X position of Core particles across the test set. **Bottom:** The coefficient of determination (R^2) versus MAE for the different hyperparameter configurations. While the Baseline Model C suffers from high variance (scatter), the Optimized Model A consistently achieves sub-resolution accuracy with a tighter error distribution, demonstrating the necessity of deeper trees to capture turbulent intermittency.

pletely independent simulation run, *u502*. Crucially, *u502* is not merely a different random realization of the turbulent velocity field; it features a different initial magnetic field strength. While the training simulation (*u501*) is strongly magnetized with a plasma beta of $\beta = 0.2$, the validation simulation (*u502*) is moderately magnetized with $\beta = 2.0$. Aside from the altered magnetic field, *u502* was initialized with identical global parameters ($\mathcal{M} = 9$, $\alpha_{\text{vir}} = 1$) but a distinct random seed, resulting in completely unique morphological structures,

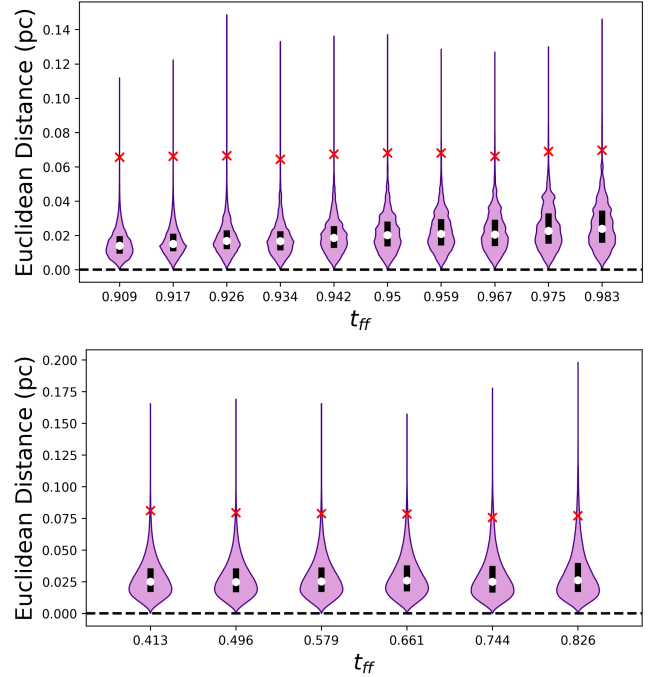


Figure 6. Temporal generalization and robustness testing. **Top:** Distribution of framewise prediction errors (Euclidean distance) for the test set within the training simulation (*u501*). The XGBoost predictions (Purple) consistently maintain lower errors than the No-Motion Baseline (Red Crosses), which assumes static particles over the prediction interval. **Bottom:** Generalization to an independent simulation run (*u502*) initialized with distinct turbulence seeds. Although the error marginally increases for the unseen simulation, the model retains predictive power (50 – 60% improvement over baseline), demonstrating that it has learned physical advection rules rather than memorizing the training volume.

such as different filament locations and core formation sites.

The bottom panel of Figure 6 illustrates the framewise prediction error when the *u501*-trained model is applied directly to *u502*. Despite the altered magnetic pressure support and different turbulent morphology, the model successfully generalizes. While the median error distribution shifts marginally higher compared to the self-consistent test, the model maintains a 50 – 60% improvement over the No-Motion baseline. It achieves a robust Mean Absolute Error of ≈ 0.012 pc and maintains a Bounded Accuracy (A_3) of over 85%. This result strongly implies that the core kinematic signatures of gravitational instability like local density enhancements coupled with convergent velocity flows, are relatively invariant across different global magnetic field strengths, allowing our purely hydrodynamic feature set to maintain predictive power. This confirms that the XGBoost

ensemble has learned the generalized physical rules of turbulent advection and collapse, rather than simply memorizing the specific spatial geometry of the training box.

4.4. Trajectory Reconstruction (Corewise Prediction)

The ultimate test for our application is the ability to reconstruct the formation history of prestellar cores. We select identifiable cores from the final simulation snapshot and recursively predict their trajectories backward and forward in time using the test set partition. To quantify the model’s reliability, we calculate the Bounded Accuracy Fraction (A_k) as defined in Eq. 13. Using a strict 3σ equivalent threshold ($k = 3$), we find that **Model A achieves an accuracy of $A_3 \approx 91\%$** . This indicates that for more than 9 out of 10 particles, the predicted trajectory lies within three times the typical model uncertainty. In contrast, the baseline Model C drops to $A_3 \approx 65\%$, indicating that nearly a third of its predictions are significant outliers. This confirms that the deeper trees in Model A are essential for capturing the intermittent, non-linear events characteristic of turbulent collapse.

Figure 7 visualizes the predicted x -position tracks (purple) versus the ground-truth simulation tracks (red) for a random sample of cores. The model successfully recovers the complex, non-linear bulk motion of the cores. Crucially, it captures the convergent flow of individual tracers as they collapse into the potential well. The strong spatial correspondence between the predicted and true mean paths confirms that the algorithm can be used as a reliable “lagrangian tracker” to identify the provenance of star-forming gas in large-scale simulations where high-frequency output might be unavailable.

5. DISCUSSION

In this work, we have demonstrated that the formation of prestellar cores in turbulent molecular clouds can be accurately forecasted using supervised machine learning. By transforming the Lagrangian history of tracer particles into a tabular regression problem, we trained an Extreme Gradient Boosting (XGBoost) model to predict 3D particle trajectories over physically significant timescales ($\sim 0.25 t_{\text{ff}}$).

Our results indicate that the local phase-space information (position, velocity, and density) contained within a single simulation snapshot holds significant predictive power regarding the future evolution of the gas. The model successfully distinguished between transient density fluctuations and gravitationally bound collapsing cores, achieving a high coefficient of determination ($R^2 > 0.99$) and recovering the convergent flow patterns of star-forming regions.

5.1. Implications for Subgrid Modeling

A primary motivation for this work is the potential to accelerate multi-scale astrophysical simulations. Current cosmological simulations (e.g., IllustrisTNG, EAGLE, FIRE) lack the resolution to follow the collapse of individual molecular cores (< 0.1 pc). Instead, they rely on heuristic “subgrid recipes” which have probabilistic criteria based on local density thresholds to spawn star particles.

Our XGBoost framework offers a data-driven alternative to these varying prescriptions. Because the inference time of a trained decision tree ensemble is negligible compared to the computational cost of solving the Poisson and MHD equations, this model could be implemented “on-the-fly” within lower-resolution simulations. By sampling tracer particles within a Giant Molecular Cloud (GMC) and passing their state vectors through the model, a simulation could statistically predict the Star Formation Rate (SFR) and the location of sink particles without needing to explicitly resolve the computationally expensive collapse phase.

Furthermore, the model’s reliance on local variables makes it potentially portable. While trained on a specific realization of solenoidal turbulence, the fundamental physics of gravitational instability captured by the decision trees (i.e., the correlation between high density, low velocity dispersion, and convergent flow) should generalize to other virialized systems.

5.2. Strengths and Limitations

5.2.1. Strengths

The primary advantage of this approach is its ability to capture **non-linear phase-space correlations** without explicit programming. Unlike analytical models that often assume spherical symmetry (e.g., Bonnor-Ebert spheres) or simple Jeans instability thresholds, XGBoost learns the complex, anisotropic geometry of turbulent accretion flows.

Additionally, the use of **Lagrangian tracer particles** is a significant improvement over Eulerian analysis for this specific task. Grid-based analysis smears out the history of the gas due to advection errors and cell mixing. By defining the problem in the Lagrangian frame, we preserve the identity of the gas parcels, allowing the ML model to “see” the coherent assembly of mass over time. This confirms that tabular machine learning methods can rival complex 3D Convolutional Neural Networks (CNNs) for specific tasks, often with significantly lower computational overhead and training data requirements.

5.2.2. Limitations

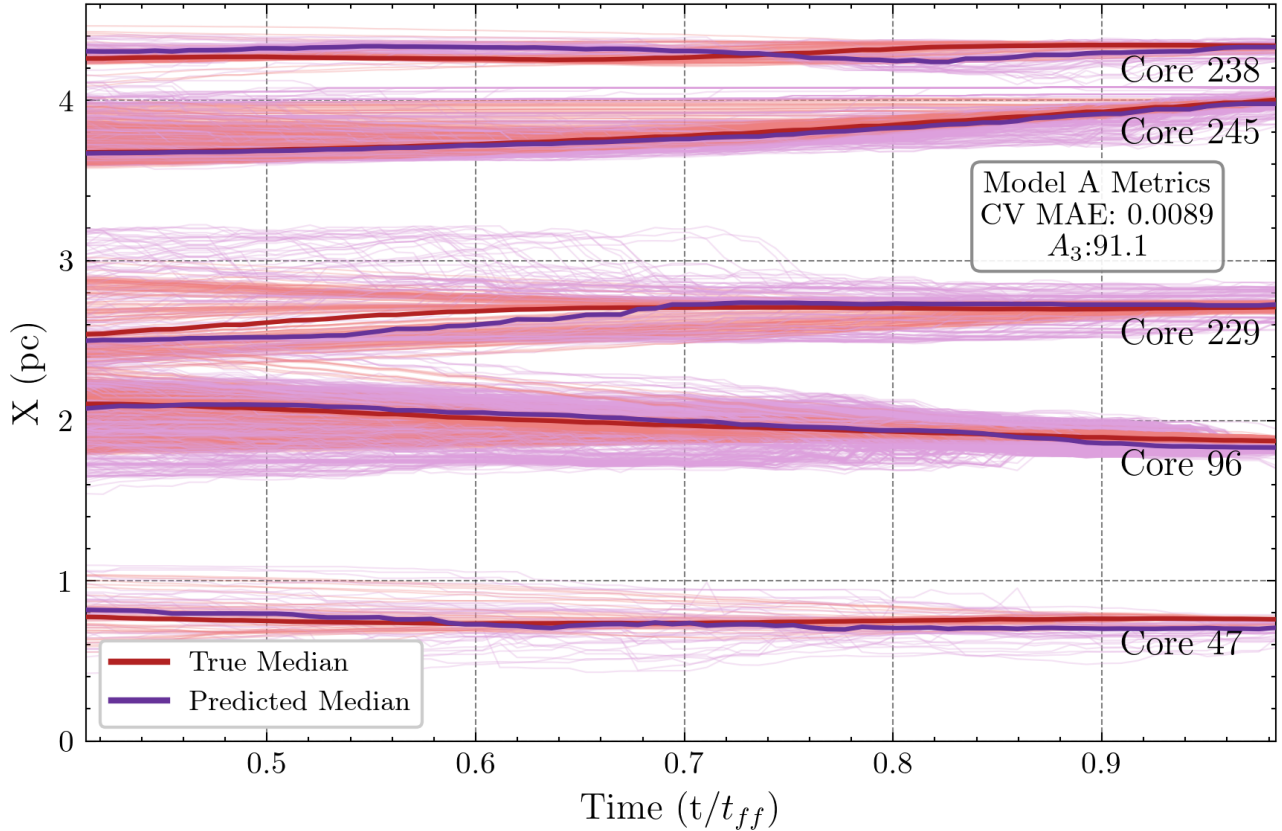


Figure 7. Trajectory reconstruction for five representative prestellar cores. The solid lines represent the median path of the constituent gas parcels (Red: Ground Truth, Purple: Model Prediction), while the faint lines show a subset of individual particle traces. The model successfully recovers the convergent flow and bulk motion of the cores over a 0.45 Myr horizon. Model A achieves a Bounded Accuracy of $A_3 \approx 91\%$, indicating that the vast majority of predicted trajectories fall within the 3σ confidence interval of the cross-validation error.

Despite its success, the model has inherent limitations common to data-driven approximations:

1. **Error Propagation:** As a regression model, errors accumulate over time. While the predictions are robust for the trained horizon ($\Delta T \approx 0.45$ Myr), recursive application of the model (predicting t_2 from t_1 , then t_3 from predicted t_2) eventually leads to divergence. This is consistent with the chaotic nature of turbulence, where the Lyapunov time limits the horizon of any deterministic prediction.
2. **Lack of Conservation Laws:** Unlike the MHD solver, XGBoost does not enforce conservation of mass, momentum, or energy. It minimizes statistical error, not physical residuals. While our "Bounded Accuracy" metric shows the results are physically plausible, there is no guarantee that two particles will not be predicted to occupy the same space in unphysical ways (though the pressure term in the training physics indirectly discourages this).

3. **Observational Applicability:** The current model relies on full 3D state vectors (x, y, z, v_x, v_y, v_z) , which are accessible in simulations but not in observations. Observers are limited to 2D projected positions and Line-of-Sight (LOS) velocities. Generalizing this framework to observational data would require retraining the model on "mock observations" (synthetic Position-Position-Velocity cubes), a logical next step for this line of research.

5.3. The Role of Magnetic Fields and Feature Selection

A notable characteristic of our XGBoost framework is that it operates exclusively on phase-space variables (position, velocity, and density) and excludes the local magnetic field vector (\mathbf{B}). In star formation theory, magnetic fields are known to provide critical pressure support against collapse, regulate the accretion rate, and channel gas along field lines, which is reflected in the macroscopic differences between our $\beta = 0.2$ and $\beta = 2.0$ simulations.

The decision to exclude **B**-field features in this initial study was driven by preliminary feature importance analyses, which indicated that the instantaneous local magnetic field strength possessed a relatively low correlation with the short-term future trajectory of the gas parcels. We hypothesize two reasons for this: First, in the highly magnetized regime ($\beta = 0.2$), the magnetic field lines are relatively stiff and uniform, meaning the variance in the field does not provide as much localized discriminative power as the highly intermittent density and velocity fields. Second, the dynamic impact of the magnetic field (e.g., magnetic pressure gradients and tension) is already implicitly encoded into the instantaneous velocity and acceleration of the gas, which the model successfully utilizes.

However, as the plasma beta increases toward the purely hydrodynamic regime (e.g., $\beta \gg 10$), the topology of the field becomes highly tangled. Applying a model trained on stiff, magnetically dominated flows ($\beta = 0.2$) to weakly magnetized turbulence would likely result in degraded performance, as the underlying rules of shock propagation and anisotropic accretion change fundamentally. While we have demonstrated robust generalization between $\beta = 0.2$ and $\beta = 2.0$, incorporating explicit magnetic field features and expanding the training set across a wider parameter space of β remains a critical avenue for future work to create a truly universal subgrid model.

6. CONCLUSION

In this paper, we presented a supervised machine learning framework to predict the trajectories and accretion history of gas in turbulent molecular clouds. By leveraging high-resolution MHD simulations and a novel Lagrangian tracer particle pipeline, we transformed the complex, non-linear problem of turbulent core collapse into a structured tabular regression task.

We successfully trained an Extreme Gradient Boosting (XGBoost) model to forecast the 3D positions of gas parcels over a horizon of ~ 0.45 Myr ($0.25 t_{\text{ff}}$). Our key findings are as follows:

1. **Predictive Power of Local Variables:** We demonstrated that the instantaneous phase-space state (density, velocity, and position) of a gas parcel contains sufficient information to predict its short-term dynamical evolution with high accuracy ($R^2 > 0.99$).

2. **Feature Importance:** Our ablation studies confirm that while density is the primary indicator of collapse, the inclusion of velocity information is critical for distinguishing between transient fluctuations and true gravitationally bound cores.

3. **Model Efficiency:** The tree-based ensemble proved to be computationally efficient and capable of handling the high dynamic range of astrophysical data without the extensive normalization required by neural networks.

This work represents a "first-order" approach, utilizing only local, point-wise information. While effective, it inherently ignores the larger morphological context—the filaments, sheets, and shock fronts—that drive large-scale flows.

6.1. Future Work

The natural extension of this work is to incorporate spatial correlations. While XGBoost is state-of-the-art for tabular data, it cannot "see" the geometry of the cloud. Future efforts will leverage Deep Learning architectures, specifically *3D Convolutional Neural Networks (CNNs)* and *Residual Networks (ResNets)*. These models can ingest the full volumetric simulation grid directly, allowing the algorithm to learn from non-local features such as filamentary convergence and magnetic field topology.

By combining the Lagrangian tracking presented here with the spatial context awareness of Deep Learning, we aim to build a unified predictive model for star formation that bridges the gap between turbulent initial conditions and final stellar populations.

ACKNOWLEDGEMENTS

Support for this work was provided in part by the National Science Foundation under Grant AAG-1616026. This work used Anvil at Purdue University (Song et al. 2022) through allocation PHY240036 from the Advanced Cyberinfrastructure Coordination Ecosystem: Services & Support (ACCESS) program, which is supported by U.S. National Science Foundation grants #2138259, #2138286, #2138307, #2137603, and #2138296 (Boerner et al. 2023).

REFERENCES

- Alatalo, K., Davis, T. A., Bureau, M., et al. 2013, Monthly Notices of the Royal Astronomical Society, 432, 1796–1844, doi: [10.1093/mnras/sts299](https://doi.org/10.1093/mnras/sts299)
- Bate, M. R., Bonnell, I. A., & Price, N. M. 1995, MNRAS, 277, 362, doi: [10.1093/mnras/277.2.362](https://doi.org/10.1093/mnras/277.2.362)

- Boerner, T. J., Deems, S., Furlani, T. R., Knuth, S. L., & Towns, J. 2023, in Practice and Experience in Advanced Research Computing (PEARC '23) (Portland, OR, USA: ACM), 1–4, doi: [10.1145/3569951.3597559](https://doi.org/10.1145/3569951.3597559)
- Bryan, G. L., Norman, M. L., O'Shea, B. W., et al. 2014, The Astrophysical Journal Supplement Series, 211, 19, doi: [10.1088/0067-0049/211/2/19](https://doi.org/10.1088/0067-0049/211/2/19)
- Chen, T., & Guestrin, C. 2016, in Proceedings of the 22nd ACM SIGKDD International Conference on Knowledge Discovery and Data Mining, KDD '16 (ACM), 785–794, doi: [10.1145/2939672.2939785](https://doi.org/10.1145/2939672.2939785)
- Chevance, M., Krumholz, M. R., McLeod, A. F., et al. 2022, The Life and Times of Giant Molecular Clouds. <https://arxiv.org/abs/2203.09570>
- Collins, D. C., Kritsuk, A. G., Padoan, P., et al. 2012, The Astrophysical Journal, 750, 13, doi: [10.1088/0004-637x/750/1/13](https://doi.org/10.1088/0004-637x/750/1/13)
- Collins, D. C., Le, D., & Jimenez Vela, L. L. 2023, MNRAS, 520, 4194, doi: [10.1093/mnras/stac2834](https://doi.org/10.1093/mnras/stac2834)
- Collins, D. C., Le, D. K., & Vela, L. L. J. 2024, Collapsing molecular clouds with tracer particles: Part II, Collapse Histories. <https://arxiv.org/abs/2306.10320>
- Collins, D. C., Xu, H., Norman, M. L., Li, H., & Li, S. 2010, ApJS, 186, 308, doi: [10.1088/0067-0049/186/2/308](https://doi.org/10.1088/0067-0049/186/2/308)
- Crutcher, R. M. 2012, araa, 50, 29, doi: [10.1146/annurev-astro-081811-125514](https://doi.org/10.1146/annurev-astro-081811-125514)
- Dieleman, S., Willett, K. W., & Dambre, J. 2015, Monthly Notices of the Royal Astronomical Society, 450, 1441–1459, doi: [10.1093/mnras/stv632](https://doi.org/10.1093/mnras/stv632)
- Evans, II, N. J., Dunham, M. M., Jørgensen, J. K., et al. 2009, ApJS, 181, 321, doi: [10.1088/0067-0049/181/2/321](https://doi.org/10.1088/0067-0049/181/2/321)
- Federrath, C., Banerjee, R., Clark, P. C., & Klessen, R. S. 2010, ApJ, 713, 269, doi: [10.1088/0004-637X/713/1/269](https://doi.org/10.1088/0004-637X/713/1/269)
- Federrath, C., & Klessen, R. S. 2012, ApJ, 761, 156, doi: [10.1088/0004-637X/761/2/156](https://doi.org/10.1088/0004-637X/761/2/156)
- Fryxell, B., Olson, K., Ricker, P., et al. 2000, ApJS, 131, 273, doi: [10.1086/317361](https://doi.org/10.1086/317361)
- Gardiner, T. A., & Stone, J. M. 2005, J. Comput. Phys, 205, 509, doi: [10.1016/j.jcp.2004.11.016](https://doi.org/10.1016/j.jcp.2004.11.016)
- Krumholz, M. R., & McKee, C. F. 2005, apj, 630, 250, doi: [10.1086/431734](https://doi.org/10.1086/431734)
- Krumholz, M. R., & Tan, J. C. 2007, ApJ, 654, 304, doi: [10.1086/509101](https://doi.org/10.1086/509101)
- Larson, R. B. 1981, mnras, 194, 809, doi: [10.1093/mnras/194.4.809](https://doi.org/10.1093/mnras/194.4.809)
- Li, S., Li, H., & Cen, R. 2008, ApJS, 174, 1, doi: [10.1086/521302](https://doi.org/10.1086/521302)
- Mac Low, M. 1999, The Astrophysical Journal, 524, 169–178, doi: [10.1086/307784](https://doi.org/10.1086/307784)
- Mac Low, M.-M., & Klessen, R. S. 2004, Reviews of Modern Physics, 76, 125, doi: [10.1103/RevModPhys.76.125](https://doi.org/10.1103/RevModPhys.76.125)
- McKee, C. F., & Ostriker, E. C. 2007, araa, 45, 565, doi: [10.1146/annurev.astro.45.051806.110602](https://doi.org/10.1146/annurev.astro.45.051806.110602)
- Mignone, A. 2007, J. Comput. Phys, 225, 1427, doi: [10.1016/j.jcp.2007.01.033](https://doi.org/10.1016/j.jcp.2007.01.033)
- Ntampaka, M., Trac, H., Sutherland, D. J., et al. 2015, ApJ, 803, 50, doi: [10.1088/0004-637X/803/2/50](https://doi.org/10.1088/0004-637X/803/2/50)
- Padoan, P., & Nordlund, Å. 2002, ApJ, 576, 870, doi: [10.1086/341790](https://doi.org/10.1086/341790)
- Peek, J. E. G., & Burkhart, B. 2019, ApJL, 882, L12, doi: [10.3847/2041-8213/ab3a9e](https://doi.org/10.3847/2041-8213/ab3a9e)
- Rosolowsky, E. W., Pineda, J. E., Kauffmann, J., & Goodman, A. A. 2008, ApJ, 679, 1338, doi: [10.1086/587685](https://doi.org/10.1086/587685)
- Sahu, D., Liu, S.-Y., & Liu, T. 2021, Frontiers in Astronomy and Space Sciences, 8, 137, doi: [10.3389/fspas.2021.672893](https://doi.org/10.3389/fspas.2021.672893)
- Shu, F. H. 1977, apj, 214, 488, doi: [10.1086/155274](https://doi.org/10.1086/155274)
- Song, X. C., Smith, P., Kalyanam, R., et al. 2022, in Practice and Experience in Advanced Research Computing 2022: Revolutionary: Computing, Connections, You, PEARC '22 (New York, NY, USA: Association for Computing Machinery), doi: [10.1145/3491418.3530766](https://doi.org/10.1145/3491418.3530766)
- Stone, M. 1974, Journal of the Royal Statistical Society: Series B (Methodological), 36, 111, doi: [10.1111/j.2517-6161.1974.tb00994.x](https://doi.org/10.1111/j.2517-6161.1974.tb00994.x)
- Tan, L., Liu, Z., Wang, X., et al. 2024, ApJS, 273, 34, doi: [10.3847/1538-4365/ad5a08](https://doi.org/10.3847/1538-4365/ad5a08)
- Wang, P., Li, Z.-Y., Abel, T., & Nakamura, F. 2009, The Astrophysical Journal, 709, 27–41, doi: [10.1088/0004-637x/709/1/27](https://doi.org/10.1088/0004-637x/709/1/27)
- Weinberger, R., Springel, V., & Pakmor, R. 2020, The Astrophysical Journal Supplement Series, 248, 32, doi: [10.3847/1538-4365/ab908c](https://doi.org/10.3847/1538-4365/ab908c)